Article

Not peer-reviewed version

Land Surface Temperature Mapping Using a Vegetation Index-Based Technique in Google Earth Engine with Multi-Temporal Remote Sensing Data

Aikaterini Stamou *

Posted Date: 21 December 2023

doi: 10.20944/preprints202312.1583.v1

Keywords: Land Surface Temperature; Land-use; NDVI; Landsat-8; Google Earth Engine

 doi:10.20944/preprints202312.1583.v1

Article

Land Surface Temperature Mapping using a Vegetation Index-based Technique in Google Earth Engine with Multi-temporal Remote Sensing data

Aikaterini Stamou [1,*]

[1] Adjunct Lecturer, School of Engineering, Aristotle University of Thessaloniki, Greece; astamoy@topo.auth.gr

* Correspondence: astamoy@topo.auth.gr

Abstract: The identified Urban Heat Island (UHI) phenomenon, coupled with diminished vegetation and anthropogenic heat release, poses a significant environmental challenge for major urban centers. Particularly worrisome is the UHI effect in hot and temperate climates such as the Mediterranean region during the summer season. This exacerbates discomfort and heightens the risks of diseases linked to high temperatures. Additionally, it contributes to environmental consequences, including elevated electricity consumption due to increased demand for cooling [1]. The utilization of Remotely Sensed imagery for estimating Land Surface Temperature has become more prevalent in various applications associated with evaluating urban micro-climates and the Urban Heat Island (UHI) phenomenon. This study presents an algorithm for the automatic mapping of Land Surface Temperature (LST) from Landsat-8 data using a vegetation index-based technique in the Google Earth Engine (GEE) platform. The primary aim is to discern patterns and trends in LST over a 5-year period, from 2017 to 2021. The application was tested in the urban area of Thessaloniki, Northern Greece, which is particularly representative of the Mediterranean urban environment. Computation of Normalized Difference Indices (NDVI, NDBI, NDWI) for the study area was also performed within the GEE platform and correlation analysis was implemented to evaluate the impact of the urban landscape on the distribution of LST.

Keywords: land surface temperature; land-use; NDVI; Landsat-8; google earth engine

1. Introduction

The heightened urbanization occurring today is contributing significantly to the urgent issue of global climate destabilization. An illustrative example of this climate change is the observed Urban Heat Island (UHI) phenomenon in urbanized regions, which arises from reduced vegetation and the discharge of anthropogenic heat. In Europe for example, approximately 73% of its population lives in cities, and by 2050 it will reach 82% [2]. The UHI phenomenon is characterized by urban areas being warmer than their surroundings. This temperature difference is typically more pronounced at night than during the day, especially in the presence of weak winds. In 2006, Oke [3], proposed four significant control factors of urban climate: '…urban structure (dimensions of the buildings and the spaces between them, street widths and street spacing), urban cover (fractions of built-up, paved, vegetated, bare soil, water), urban fabric (construction and natural materials), and urban metabolism (heat, water and pollutants due to human activity)'. The modification of all these factors that follows the urban development, cause the UHI effect.

Typically, the intensity of UHI effect becomes particularly critical in cities lacking effective landscaping. In such urban areas, issues related to heat islands, including increased energy consumption, reduced air quality, and impacts on human health and mortality, become increasingly urgent [4]. UHI is one of the precarious environmental challenges that modern cities face nowadays and has been the subject matter in many scientific studies [5–7].

O'Malley et al. [8] explored strategies for mitigating UHI that are both effective and resilient, aiming to offer guidance for their future implementation. Harlan S. et al. [9] have summarized studies on mortality and morbidity associated with two urban climate hazards: rising temperatures and the

 doi:10.20944/preprints202312.1583.v1

altering impact of air pollution. The objective is to propose strategies for both mitigation and adaptation, with the aim of generating health co-benefits. Tan, J. et al. [10] noted in their study that 'UHI effect may potentially increase the magnitude and duration of extreme events such as heat waves'. In European Region heatwaves are becoming more frequent and more intense [11]. Sidewise, UHI leads to a notable surge in energy consumption, attributed to the increased usage of cooling systems in both commercial and residential buildings [12]. This is a growingly alarmed issue for European Governments due to the energy crisis that was evident the previous winter (2022-2023) and it is expected to remain the following years.

Various urban cooling methodologies have been proposed, including enhancing the surface reflectivity of urban materials [13–15] or the enhancement of urban vegetation with green spaces or even green roofs [16–19] to facilitate the decrease of the UHI effect.

In order to investigate and apply these strategies in urban environments, with the intention of controlling and minimizing the UHI effect, it is important to perform an accurate detection and estimation of urban area development, including its direction, especially in conjunction with microclimate parameters such as Land Surface Temperature (LST). Employing Remote Sensing techniques for extracting LST and conducting spatio-temporal analyzes of urban development can significantly techniques can effectively contribute to UHI analysis. Relevant studies have initially practiced extraction of LST us-ing medium resolution sensors of Landsat ETM+ and ASTER [20–23]. During the last decade, Landsat 8 from 2013, and recently Landsat 9 from 2021, allowed scientists to acquire free, high credential satellite data with revisit time for data collection every 8 days, giving the opportunity to assess and monitor accurately land cover and land use and study diachronically their interaction with LST. Additionally, Landsat 8 and Landsat 9 exhibit superior radiometric and geometric characteristics compared to earlier generations of Landsat satellites. [23].

Numerus Remote Sensing techniques have been proposed with different approaches to obtain LST from satellite data, using various methods to address emissivity and atmospheric effects [24–28]. In this work an algorithm for the automatic mapping of LST from LANDSAT 8 data is presented within Google Earth Engine (GEE), applying a vegetation adjustment using Landsat-derived Normalized Difference Vegetation Index (NDVI), alongside with the Fraction Vegetation Cover (FVC) [29,30]. Continuously the NDVI thresholds method [27,29], [31], was successfully applied for calculating surface emissivity that is used for the LST calculation. The advantage of GEE platform is that it allows users to access and process time-series Remotely Sensed data without increasing the demand for local storage space. The application was tested in the urban area of Thessaloniki (Northern Greece), analyzing the urban albedo and its impact on LST over the last 5 years, from 2017 to 2021.

2. Materials and Methods

2.1. Study area

Thessaloniki is a densely populated urban area located in a coastal area of the North-ern part of Greece (DMS latitude and longitude coordinates: 40° 37' 45.3684'' N, 22° 56' 50.6832'' E) (Figure 1). The greater area of Thessaloniki is home to a population exceeding one million residents. It is surrounded by relatively high mountain in the East-Northeast, with Mount Hortiatis, a nearly flat terrain in the West, and the Thermaikos Gulf to the South. [32].

Thessaloniki's climate is warm and temperate, with average annual temperature 15.4 °C, where July is the warmest month of the year with average temperature 26.6 °C and January has the lowest average temperature of the year (4.2°C) [33].

The urban albedo comprises both old and more recent developed areas, characterized by high and low built-up density respectively, with a continuous increase of impervious land surfaces over the last decades.

 doi:10.20944/preprints202312.1583.v1

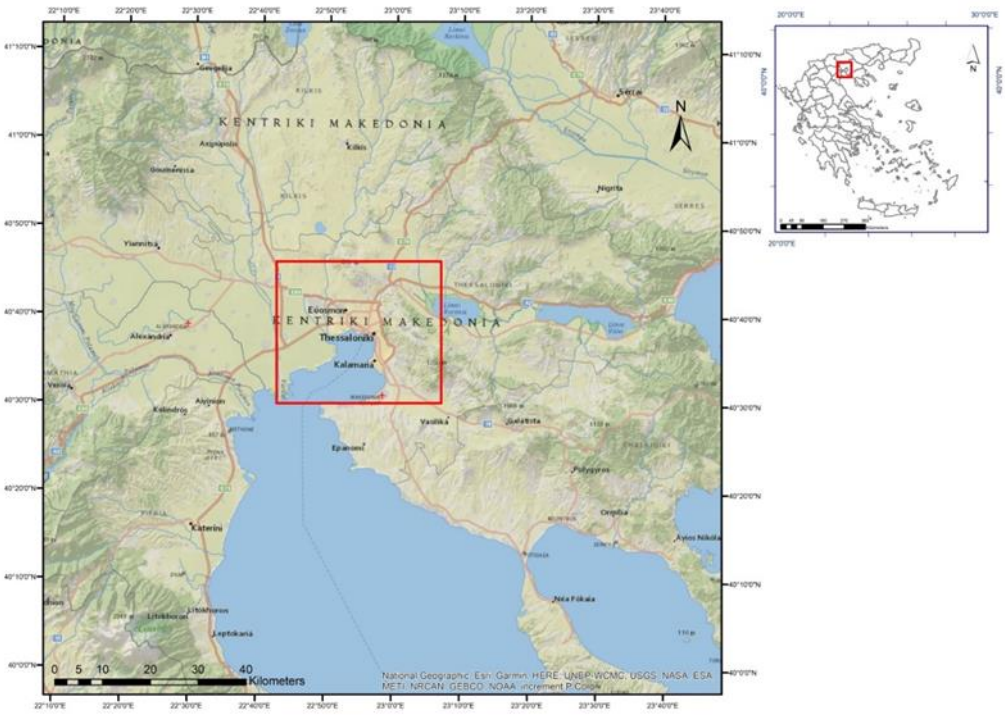

Figure 1. Study area of Thessaloniki, Greece (base map: National Geographic, ESRI).

2.2. Input data

GEE platform provides a wide range of Landsat satellite images, produced by the USGS (United States Geological Survey) and for this research, Landsat 8 time series data were used. Landsat 8 Operational Land Imager (OLI) and Thermal Infrared Sensor (TIRS) images consist of nine spectral bands with a spatial resolution of 30 meters for Bands 1 to 7 and 9. TIRS gathers data from two narrower spectral bands in the thermal region, which was initially covered by a single wide spectral band on Landsat 4–7. The 100-meter TIRS data is registered to the OLI data, resulting in radiometrically, geometrically, and terrain-corrected 12-bit data products. These products are valuable for delivering more precise surface temperature information. [23]. The USGS produces data in tiers (categories) based on their quality; Tier 1 (T1) - data that meets geo-metric and radiometric quality requirements, Tier 2 (T2) - data that doesn't meet the Tier 1 requirements and Real Time (RT) - data that hasn't yet been evaluated. GEE has grouped the scenes into collections by tiers and satellites to facilitate users. This research used Tier 1 Landsat 8 data. Table 1 shows the properties of Landsat 8 data available in GEE collections. (Table 1)

Table 1. Landsat 8 properties.

Satellite	Bands	Wavelength (μm)	Spatial Resolution (m)	Date Range
Landsat-8	B1	0.433–0.453	30	April 13- present
	B2	0.450–0.515	30	
	B3	0.525–0.600	30	
	B4	0.630–0.680	30	
	B5	0.845–0.885	30	
	B6	1.560–1.660	30	
	B7	2.100–2.300	30	
	B8	0.500–0.680	15	
	B9	1.360–1.390	30	
	B10	10.6-11.2	100 [1]	
	B11	11.5-12.5	100 [1]	

 doi:10.20944/preprints202312.1583.v1

QA (Quality Assessment band)	30

[1] Resampled to 30m.

2.3. *LST extraction*

LST estimation was carried out using the NDVI-based emissivity method (NBEM). Norman and Becker [34] defined land surface emissivity as: 'a wavelength-dependent quantity: the ratio of the radiance actually emitted by an isothermal, homogeneous body and the radiance emitted by a black body at the same thermodynamic temperature'. In effect, it represents the surface's capacity to convert heat energy into radiant energy [35]. Using the NDVI-based emissivity method, emissivity is defined as a function of the Normalized Difference Vegetation Index. Land cover type and land use have a significant impact on surface emissivity [36], therefore NDVI-based methods are frequently utilized in LSE retrieval methods [27], [35], [37–39] as NDVI can demonstrate effectively the different types of land surfaces.

With the NBEM, the NDVI-adjusted emissivity – εNDVI [26,27], [39,40] is calculated using the equation:

$$\varepsilon NDVI = FVC * \varepsilon_{veg} + (1 + FVC) * \varepsilon_{bare}, \quad (1)$$

where ε_{veg} and ε_{bare} are the emissivity of vegetation and bare ground for a given spectral band and FVC is the Fractional Vegetation Cover and is calculated with the relationship proposed by Carlson and Ripley [29]:

$$FVC = (NDVI - NDVI_{max}) / (NDVI_{min} - NDVI_{max}), \quad (2)$$

where $NDVI_{min}$ and $NDVI_{max}$ depict the minimum and the maximum NDVI values of a given study area respectively.

As the study area is mainly urban area with rural surfaces in its surroundings, the ε_{veg} and ε_{bare} values in equation (1) were adjusted to ε_{veg} and ε_{urban}. The ε_{veg} was set to 0.99 because of the limited variability observed for vegetated surfaces and ε_{urban} was set in 0.970 as suggested by Chakraborty et al. [39].

The LST can be derived using the inverse Planck's law equation:

$$LST = Tb / [1 + \{(\lambda * Tb / \varrho) * \ln \varepsilon] - 273.15, \quad (3)$$

where: LST is the LST in Celsius (°C), Tb is the TOA brightness temperature in the TIR channel TR (°C), λ is the wavelength of emitted radiance (for which the peak response and the average of the limiting wavelength for Landsat 8 band 10 (λ = 10.9μm) will be used.

$$\varrho = h * c/\sigma \ (1.438 * 10^{-2} mK), \quad (4)$$

where σ = Boltzmann constant ($1.38 * 10^{-23}$ J/K), h = Planck's constant ($6.626 * 10^{-34}$ Js), c = velocity of light ($2.998 * 10^{8}$ m/s), ε = the emissivity calculated in previous steps from equation (1).

2.4. *GEE implementation*

All the above-mentioned procedures were implemented in GEE platform. First, time series of Landsat 8 images were collected; the time series data were divided into five annual periods for the years 2017, 2018, 2019, 2020, 2021. For all image collections, clouds and cloud shadows were screened and removed using the quality information bands. Continuously, the NDVI was calculated based on the following equation:

$$NDVI = (NIR - RED) / (NIR + RED), \quad (5)$$

where RED and NIR represent the spectral reflectance values obtained from the red (visible) and near-infrared regions, respectively. The median NDVI for each annual time-series dataset was then calculated. Watery parts of the study area were also excluded by calculating the Normalized Difference Water Index (NDWI) using the Shortwave Infrared and Green band:

$$NDWI = (GREEN - SWIR) / (GREEN + SWIR), \quad (6)$$

where GREEN and SWIR represent spectral reflectance values acquired from the Green and Near Shortwave Infrared regions of Landsat 8, respectively. The minimum and maximum of NDVI values were then calculated for every year, and assigned to the FVC equation (equation 2) and

 doi:10.20944/preprints202312.1583.v1

subsequent estimate the NDVI-adjusted emissivity (equation 1) for every year. Finally, the LST estimation was derived from equation (3).

3. Results

3.1. LST distribution

The derived results are displayed in Figure 2 with charts of LST values that were calculated from the image composites for the five reference years (2017 to 2021).

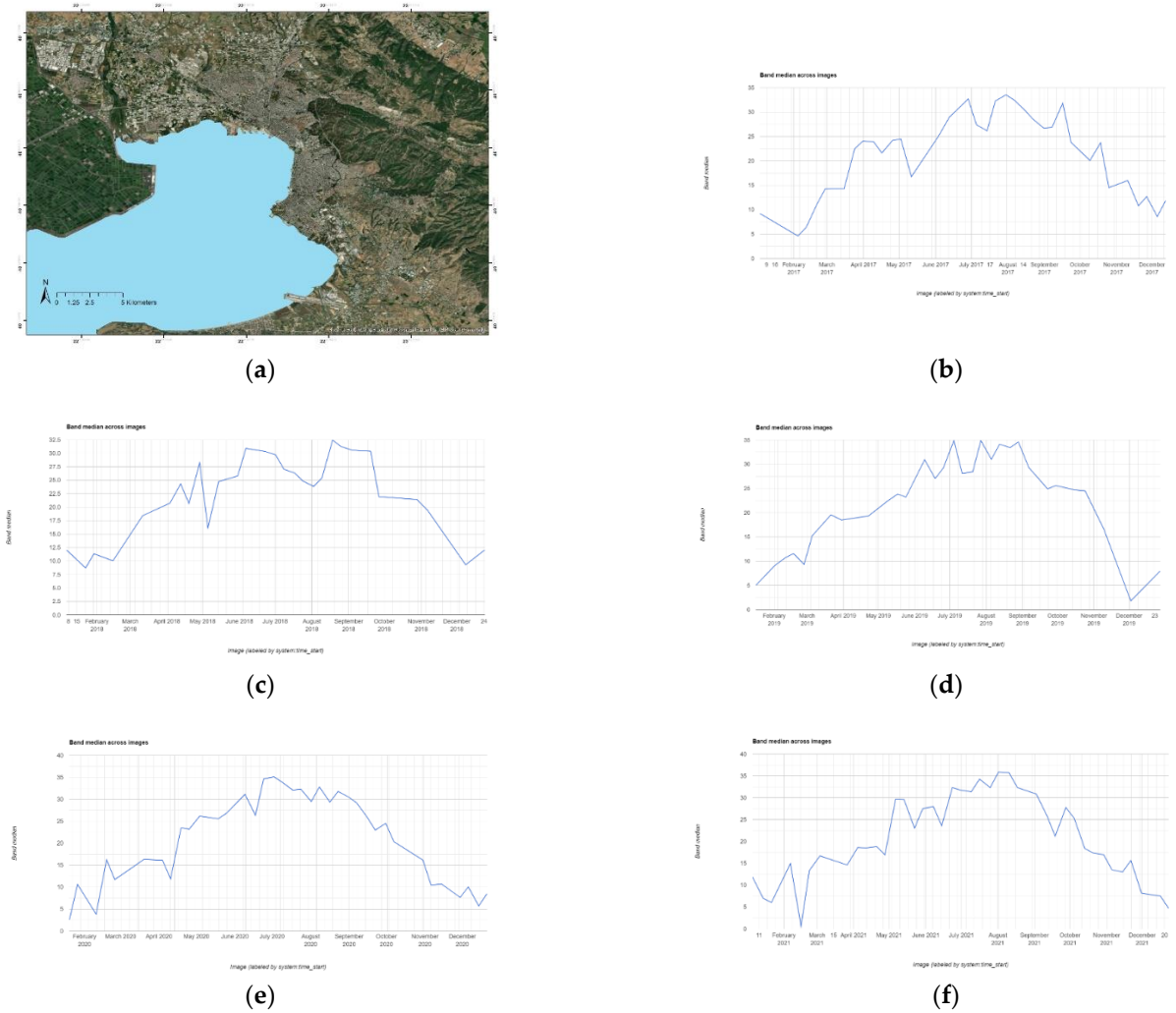

Figure 2. (a) The satellite image of the study area and median LST values derived from Landsat 8 data over the years of; (b) 2017; (b) 2018; (c) 2019; (d) 2020; (f) 2021.

The charts reflect that, as expected for a Mediterranean region, the period from July to September has the highest LST values for all five reference annual periods, and on the other hand on January and December the LST appears to have its lowest values.

To thoroughly investigate the intensity of UHI and its variations from 2017 to 2021, we employed vector data analysis, incorporating zonal statistics and descriptive statistics. The spatial representation of Land Surface Temperature (LST) throughout the studied period (Figure 3) sums up the outlines of LST variation for every reference year. The lowest annual surface temperature occurred in 2021 with an average surface temperature of 23.18°C, while the highest annual temperature occurred in 2019 with an average surface temperature of 25.78°C. Peak values for the highest observed temperatures appeared in 2020 (40.77°C) and lowest observed temperatures both in 2018 and 2021 (11.05°C) (Table 2). Additionally, the LST images reveal patterns of LST distribution

 doi:10.20944/preprints202312.1583.v1

over the examined area; The dense urban tissue of Thessaloniki has higher observed LST values than its suburban surroundings and the rural/mountainous areas confirming the UHI effect.

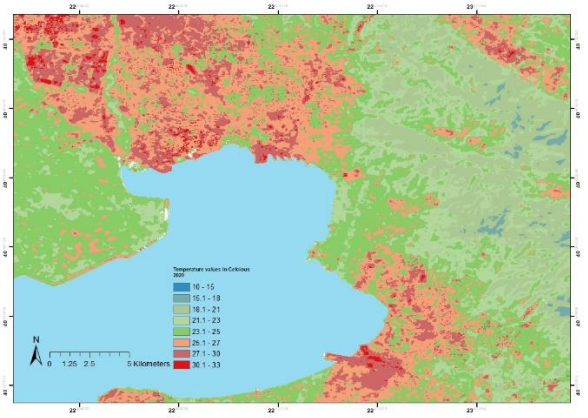

(a)

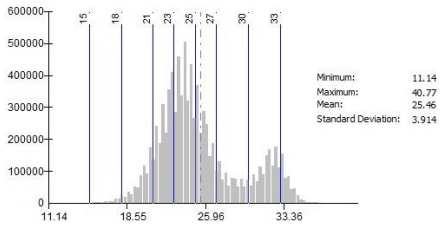

(b)

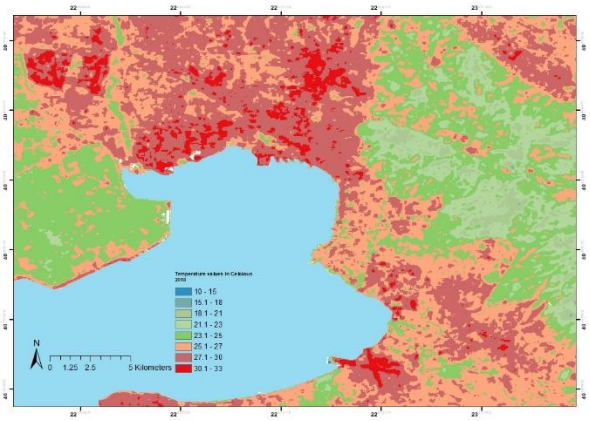

(c)

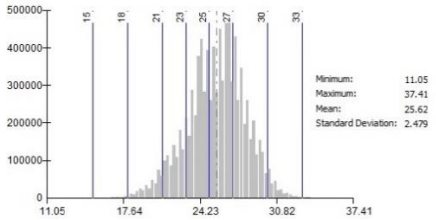

(d)

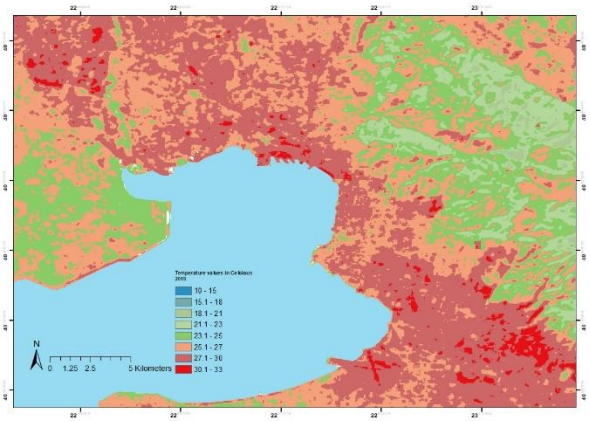

(e)

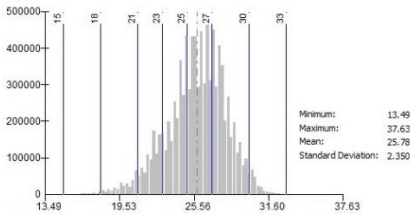

(f)

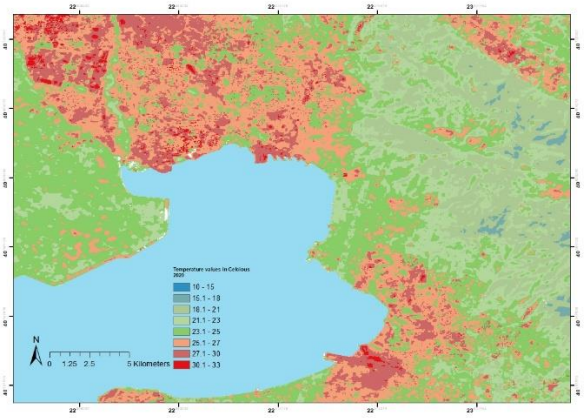

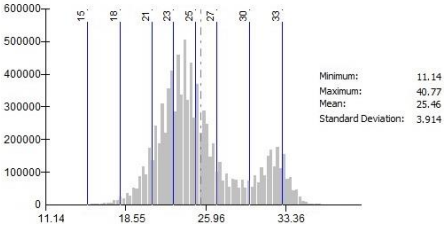

 doi:10.20944/preprints202312.1583.v1

(g) **(h)**

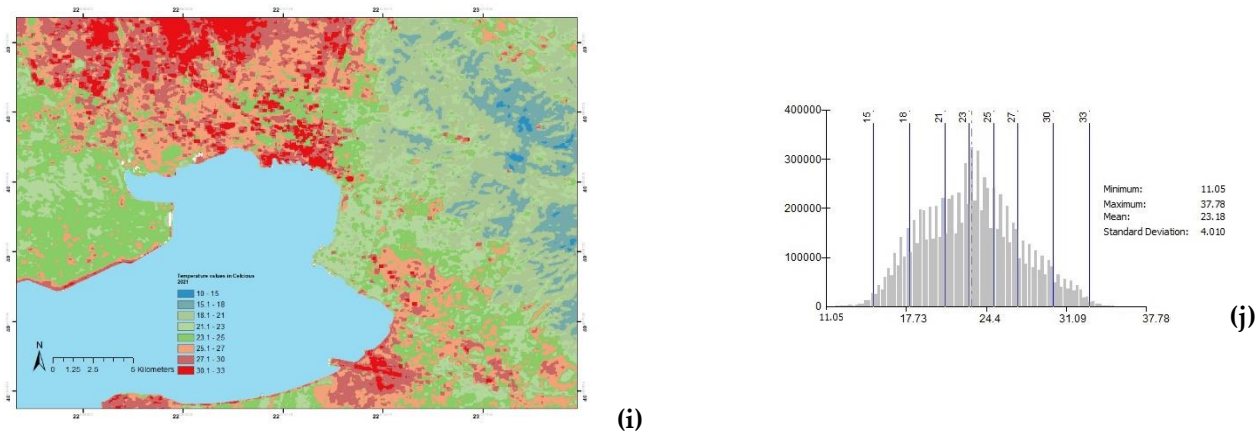

(i) **(j)**

Figure 3. The derived LST images of the area of interest and their resulting statistical data over the five-year period: (**a**) and (**b**) for 2017; (**c**) and (**d**) for 2018; (**e**) and (**f**) for 2019; (**g**) and (**h**) for 2020; (**i**) and (**j**) for 2021.

Table 2. Minimum, maximum, mean values and standard deviation for LST derived by the image composites for the reference years of 2017-2021.

LST (°C)				
Year	Min	Max	Average	Standard deviation
2017	11.65	34.63	24.72	2.52
2018	11.05	37.41	25.62	2.47
2019	13.49	37.63	25.78	2.35
2020	11.14	40.77	25.46	3.91
2021	11.05	37.78	23.18	4.01

Additionally, the LST images accurately detected and highlighted thermal hotspots within the study area; for example, the area of airport runways (Figure 4). It is worth mentioning that LST images of 2017 and 2020 show that runways had noteworthy lower LST values as during 2017 Macedonia Airport was undergoing renovation works and during 2020 the airport was underperforming for a large period of time due to Covid 19 restrictions.

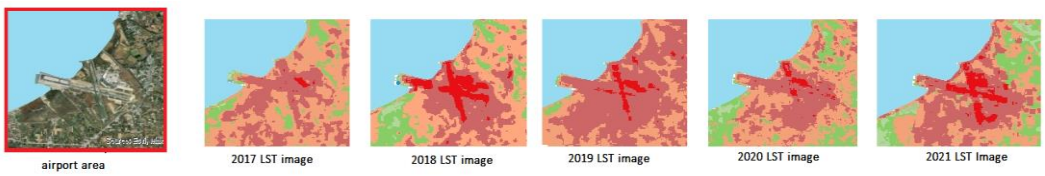

Figure 4. Airport area. Detail of the initial satellite image and the produced LST images for the years 2017-2021.

3.2. LST correlation with different land uses

UHI phenomenon can be easily detected when comparing LST values with different land uses. For this purpose, CORINE Land Cover (CLC) classes of 2018 were used. CORINE Land Cover provides land use and land cover (LULC) datasets, monitoring at the pan-European level and is running under the Copernicus programme which is the Euro-pean Union's Earth observation programme. Nine CORINE Land Cover classes were identified in the study area: Continuous urban fabric, Industrial and Commercial units, Rail, Airport areas, Mineral extraction sites/Construction sites, Agricultural land, Forest, Natural Grassland and Wetlands (Figure 5).

Preprints.org (www.preprints.org) | NOT PEER-REVIEWED | Posted: 21 December 2023 doi:10.20944/preprints202312.1583.v1

Figure 5. CORINE Land Cover Classes distribution map.

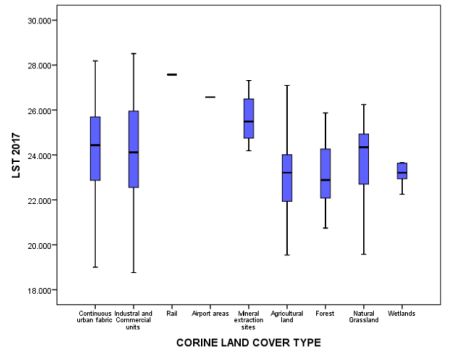

(**a**)

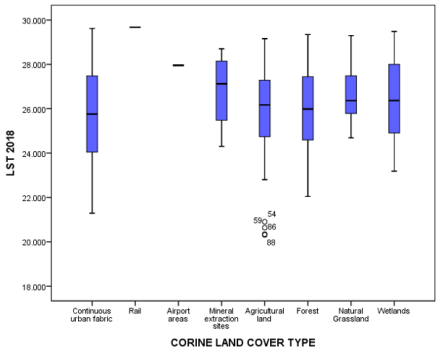

(**b**)

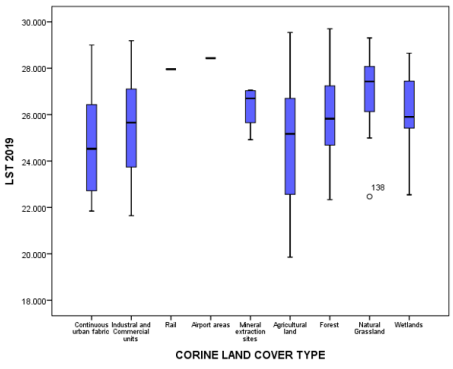

(**c**)

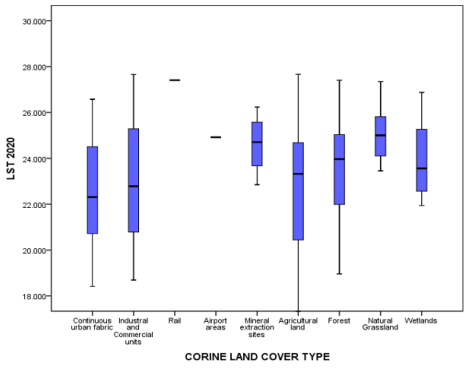

(**d**)

 doi:10.20944/preprints202312.1583.v1

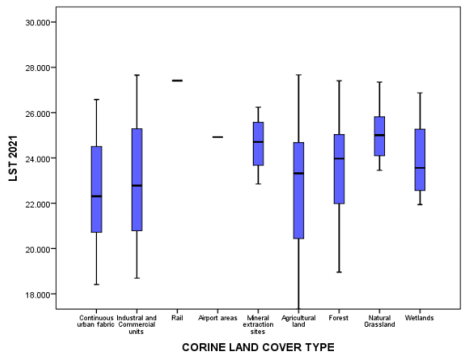

(**e**)

Figure 6. Boxplots of CORINE Land Cover Classes with their LST values: (**a**) for year 2017, (**b**) for year 2018, (**c**) for year 2019, (**d**) for year 2020, (**e**) for year 2021.

Boxplots were produced for all CLC classes that were identified within the study area (Figure 6) showing the distribution of LST values and the skewness for every class. The boxplots of classes that contain mainly built-up areas (Continuous urban fabric, Industrial and Commercial units, Rail, Airport areas, Mineral extraction sites/Construction sites) are positively skewed as their median value tends to be closer to the upper quartile value meaning that LST has higher values than the average value, while classes that contain mainly bare soil and green areas or water (Agricultural land, Forest, Natural Grassland, Wetlands) their boxplots have negative skewness as their median value tends to be closer to the lower quartile value. What is also notable is the wider dispersion of LST values of Agricultural land class for all five reference years.

3.3. LST correlation with NDVI

The UHI phenomenon can also be identified and interpretated by examining the relationship between LST values of NDVI index within the LULC datasets. Scatterplots were produced between mean values of LST and mean values of NDVI in every LULC dataset for the reference years 2017 to 2021 and the correlation coefficient was also calculated for the examined couples (LST-NDVI). The results are showed in Figure 7 and Table 3.

The results indicate a moderately strong, negative, linear correlation between the examined LULC datasets and the two variables. However, there are a few potential outliers for the reference years 2018, 2019, 2020, and 2021. Conversely, for the reference year 2017, a weak negative linear association is observed between the two variables. The Pearson correlation results show correlation values ranging from -0.82 to -0.33 between NDVI and surface temperature for the LULC, and this correlation is statistically significant at the 0.01 level for all reference years.

 doi:10.20944/preprints202312.1583.v1

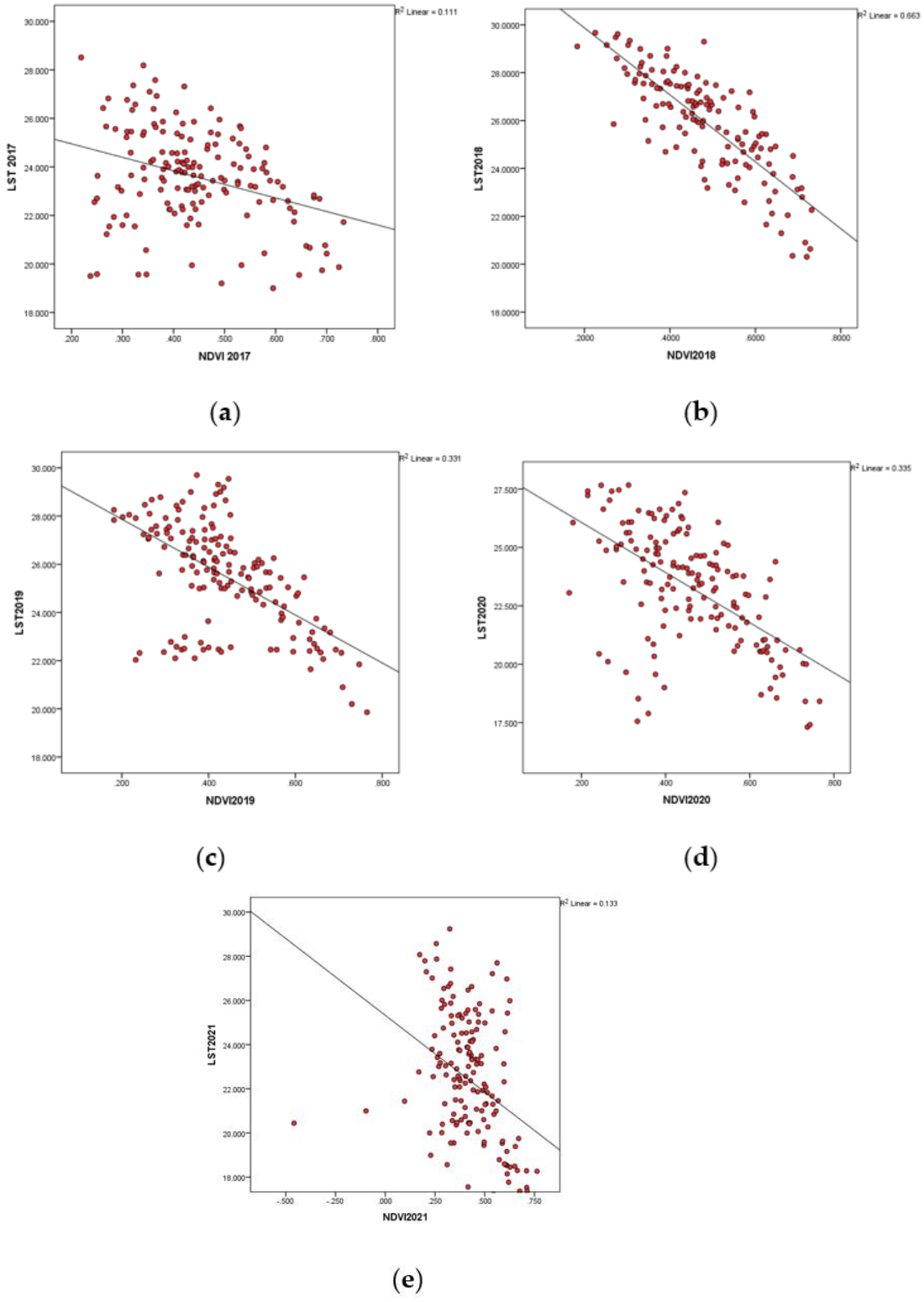

Figure 7. Scatterplots between LST and NDVI for the reference years of: (a) 2017, (b) 2018, (c) 2019, (d 2020, (e) 2021.

 doi:10.20944/preprints202312.1583.v1

Table 3. Pearson Correlation results between LST and NDVI for the reference years of 2017-2021.

Mean LST values with Mean NDVI values correlation	
Year	**Pearson Correlation**
2017	-.333**
2018	-.814**
2019	-.575**
2020	-.579**
2021	-.364**
**. Correlation is significant at the 0.01 level (2-tailed).	

4. Discussion

The primary goal of this project is the assessment of the vegetation-indexed LST estimates from LANDSAT 8 data using the platform of GEE, focusing on identifying LST patterns or trends within a 5-year period from 2017 to 2021. The results revealed that the average LST values for the whole examined area have risen nearly 1°C (from 24.72°C of 2017 to 25.46°C of 2021) and at the same time the peak values of surface temperature were found to have risen 5°C within the examined 5-year period (from 34.63°C of 2017 to 40.77°C of 2021). Distinct difference is identified in different LULC datasets of the study area, where pervious green areas or areas of water (Agricultural land, Forest, Natural Grassland, Wetlands) possess lower LST values than the impervious LULC dataset with dense settlements and lack of vegetation namely: Continuous urban fabric, Industrial and Commercial units, Rail, Airport areas, Mineral extraction sites/Construction sites.

The cross-correlation of LST and NDVI index within these LULC datasets revealed a moderate negative, linear relationship between these variables, high-lighting once more that pervious areas mainly covered by vegetation compared to impervious areas tend to have lower temperature values. Since correlation between Land Surface Temperature (LST) and air temperature displays a spatial distribution pattern similar to what has been documented in previous studies [38,41–50], this recognized patterns and trends over the examined area throughout the 5-year period could contribute to climate monitoring and therefore assist in UHI scenarios with the visualization of its spatial distribution trends and patterns.

As the 2030 Agenda for Sustainable Development of the United Nations [51] suggest that practical solutions that can accelerate progress on the Sustainable Development Goals (SDGs) are urgently needed, incorporating climate change measures into national policies, strategies, and planning is crucial. It is always challenging to identify and implement key measures that lead to climatic resilience and climate monitoring plays an important role. Remote Sensing contributes to effective climate monitoring as it offers the continuous assessment of spatial distribution trends; in our case the LST variation over the urban and suburban areas of Thessaloniki in Greece. It provides information over areas where there is not a ground monitoring station available, the visualization offers a quick and easy interpretation and data can be examined retrospectively in order to assess and identify a trend over the years. With the suggested methodology, the open-source data was used within the GEE platform, where the resulting code can be easily customized to a different area of interest and at the same time widen the retrospective time period.

Thessaloniki has witnessed rapid growth and ongoing developments in both its urban and peri-urban areas. It is essential to evaluate the repercussions of this urban expansion to strengthen its climatic resilience. The current study with the LST distribution over a 5-year period could contribute towards this goal as it facilitates and suggests the impact of this urbanization on the area's urban climate. Nature-based actions and solutions, targeting 'underprivileged' areas where a lack of vegetation and higher values of LST are observed with this methodology could contribute to this climate change adaptation. Future studies could explore the integration of ground air temperature data from the study area to validate the findings and enhance their credibility.

 doi:10.20944/preprints202312.1583.v1

Institutional Review Board Statement: Not applicable.

Data Availability Statement: Publicly available datasets were analyzed in this study. This data can be found here: https://developers.google.com/earth-engine/datasets.

Conflicts of Interest: The authors declare no conflict of interest.

References

1. Desideri, U.; Francesco Asdrubali. *Handbook of Energy Efficiency in Buildings*; 2019. https://doi.org/10.1016/c2016-0-02638-4.
2. United Nations; Department of Economic and Social Affairs. *World Urbanization Prospects 2018 Highlights*; 2018.
3. Oke, T. R. Towards Better Scientific Communication in Urban Climate. *Theor. Appl. Climatol.* **2006**, *84* (1–3), 179–190. https://doi.org/10.1007/s00704-005-0153-0.
4. Lisa Gartlant. Heat Islands: Understanding and Mitigating Heat in Urban Areas. *Earthscan Lond. UK* **2008**, 192. https://doi.org/10.1080/07293682.2011.591742.
5. Bonafoni, S.; Baldinelli, G.; Verducci, P. Sustainable Strategies for Smart Cities: Analysis of the Town Development Effect on Surface Urban Heat Island through Remote Sensing Methodologies. *Sustain. Cities Soc.* **2017**, *29*, 211–218. https://doi.org/10.1016/j.scs.2016.11.005.
6. Li, X.; Mitra, C.; Dong, L.; Yang, Q. Understanding Land Use Change Impacts on Microclimate Using Weather Research and Forecasting (WRF) Model. *Phys. Chem. Earth* **2018**, *103*, 115–126. https://doi.org/10.1016/j.pce.2017.01.017.
7. Wang, W.; Liu, K.; Tang, R.; Wang, S. Remote Sensing Image-Based Analysis of the Urban Heat Island Effect in Shenzhen, China. *Phys. Chem. Earth* **2019**, *110*, 168–175. https://doi.org/10.1016/j.pce.2019.01.002.
8. O'Malley, C.; Piroozfarb, P. A. E.; Farr, E. R. P.; Gates, J. An Investigation into Minimizing Urban Heat Island (UHI) Effects: A UK Perspective. *Energy Procedia* **2014**, *62*, 72–80. https://doi.org/10.1016/j.egypro.2014.12.368.
9. Harlan, S. L.; Ruddell, D. M. Climate Change and Health in Cities: Impacts of Heat and Air Pollution and Potential Co-Benefits from Mitigation and Adaptation. *Curr. Opin. Environ. Sustain.* **2011**, *3* (3), 126–134. https://doi.org/10.1016/J.COSUST.2011.01.001.
10. Tan, J.; Zheng, Y.; Tang, X.; Guo, C.; Li, L.; Song, G.; Zhen, X.; Yuan, D.; Kalkstein, A. J.; Li, F.; Chen, H. The Urban Heat Island and Its Impact on Heat Waves and Human Health in Shanghai. *Int. J. Biometeorol.* **2010**, *54* (1), 75–84. https://doi.org/10.1007/s00484-009-0256-x.
11. Heaviside, C.; Vardoulakis, S.; Cai, X. M. Attribution of Mortality to the Urban Heat Island during Heatwaves in the West Midlands, UK. *Environ. Health Glob. Access Sci. Source* **2016**, *15*. https://doi.org/10.1186/s12940-016-0100-9.
12. Vujovic, S.; Haddad, B.; Karaky, H.; Sebaibi, N.; Boutouil, M. Urban Heat Island: Causes, Consequences, and Mitigation Measures with Emphasis on Reflective and Permeable Pavements. *CivilEng* **2021**, *2* (2), 459–484. https://doi.org/10.3390/civileng2020026.
13. Yuan's Lab, J.; Yuan, J.; Masuko, S.; Shimazaki, Y.; Chai, J. Researching the Design of a Glass-Bead Retro-Reflective Material to Reduce Downward Reflection for Urban Heat Island Mitigation. *Mater. Today Sustain.* **2022**, *18* (1). https://doi.org/10.1016/j.mtsust.2022.100147Lab.
14. Cedillo-González, E. I.; Governatori, M.; Ferrari, C.; Siligardi, C. Solar Reflective Ink-Jet Printed Porcelain Stoneware Tiles as an Alternative for Urban Heat Island Mitigation. *J. Eur. Ceram. Soc.* **2022**, *42* (2), 707–715. https://doi.org/10.1016/J.JEURCERAMSOC.2021.10.045.
15. Pham, J. V.; Baniassadi, A.; Brown, K. E.; Heusinger, J.; Sailor, D. J. Comparing Photovoltaic and Reflective Shade Surfaces in the Urban Environment: Effects on Surface Sensible Heat Flux and Pedestrian Thermal Comfort. *Urban Clim.* **2019**, *29*, 100500. https://doi.org/10.1016/J.UCLIM.2019.100500.
16. Zuo, J.; Ma, J.; Lin, T.; Dong, J.; Lin, M.; Luo, J. Quantitative Valuation of Green Roofs' Cooling Effects under Different Urban Spatial Forms in High-Density Urban Areas. *Build. Environ.* **2022**, *222*, 109367. https://doi.org/10.1016/J.BUILDENV.2022.109367.
17. Wang, Y.; Akbari, H. Analysis of Urban Heat Island Phenomenon and Mitigation Solutions Evaluation for Montreal. *Sustain. Cities Soc.* **2016**, *26*, 438–446. https://doi.org/10.1016/j.scs.2016.04.015.
18. Jim, C. Y.; Hui, L. C. Offering Green Roofs in a Compact City: Benefits and Landscape Preferences of Socio-Demographic Cohorts. *Appl. Geogr.* **2022**, *145*. https://doi.org/10.1016/j.apgeog.2022.102733.
19. Lin, M.; Dong, J.; Jones, L.; Liu, J.; Lin, T.; Zuo, J.; Ye, H.; Zhang, G.; Zhou, T. Modeling Green Roofs' Cooling Effect in High-Density Urban Areas Based on Law of Diminishing Marginal Utility of the Cooling Efficiency: A Case Study of Xiamen Island, China. *J. Clean. Prod.* **2021**, *316*, 128277. https://doi.org/10.1016/J.JCLEPRO.2021.128277.
20. Zhang, Y.-P.; He, Y.-L.; Liu, Y.-H.; MAYou-Xin, M. A.; Li, Y.-R.; Jun-Xia, D. *Thermal Effects Of Building's External Surfaces In City-Characteristics of Heat Flux into and out of External Wall Surfaces*; Science Press, 2004; Vol. 14, pp 343–349.

 doi:10.20944/preprints202312.1583.v1

21. Liu, K.; Su, H.; Zhang, L.; Yang, H.; Zhang, R.; Li, X. Analysis of the Urban Heat Island Effect in Shijiazhuang, China Using Satellite and Airborne Data. *Remote Sens.* **2015**, *7* (4), 4804–4833. https://doi.org/10.3390/rs70404804.
22. Weng, Q.; Hu, X.; Quattrochi, D. A.; Liu, H. Assessing Intra-Urban Surface Energy Fluxes Using Remotely Sensed ASTER Imagery and Routine Meteorological Data: A Case Study in Indianapolis, U.S.A. *IEEE J. Sel. Top. Appl. Earth Obs. Remote Sens.* **2014**, *7* (10), 4046–4057. https://doi.org/10.1109/JSTARS.2013.2281776.
23. Landsat Science. *Landsat Science*. LANDSAT 9. https://landsat.gsfc.nasa.gov/satellites/landsat-9/ (accessed 2023-04-06).
24. Li, Z. L.; Tang, B. H.; Wu, H.; Ren, H.; Yan, G.; Wan, Z.; Trigo, I. F.; Sobrino, J. A. Satellite-Derived Land Surface Temperature: Current Status and Perspectives. *Remote Sens. Environ.* **2013**, *131*, 14–37. https://doi.org/10.1016/J.RSE.2012.12.008.
25. Sekertekin, A.; Bonafoni, S. Sensitivity Analysis and Validation of Daytime and Nighttime Land Surface Temperature Retrievals from Landsat 8 Using Different Algorithms and Emissivity Models. *Remote Sens.* **2020**, *12* (17). https://doi.org/10.3390/RS12172776.
26. Avdan, U.; Jovanovska, G. Algorithm for Automated Mapping of Land Surface Temperature Using LANDSAT 8 Satellite Data. *J. Sens.* **2016**, *2016*. https://doi.org/10.1155/2016/1480307.
27. Ermida, S. L.; Soares, P.; Mantas, V.; Göttsche, F. M.; Trigo, I. F. Google Earth Engine Open-Source Code for Land Surface Temperature Estimation from the Landsat Series. *Remote Sens.* **2020**, *12* (9). https://doi.org/10.3390/RS12091471.
28. Sobrino, J. A.; El Kharraz, J.; Li, Z. L. Surface Temperature and Water Vapour Retrieval from MODIS Data. *Int. J. Remote Sens.* **2003**, *24* (24), 5161–5182. https://doi.org/10.1080/0143116031000102502.
29. Carlson, T. N.; Ripley, D. A. On the Relation between NDVI, Fractional Vegetation Cover, and Leaf Area Index. *Remote Sens. Environ.* **1997**, *62* (3), 241–252. https://doi.org/10.1016/S0034-4257(97)00104-1.
30. Zhang, S.; Chen, H.; Fu, Y.; Niu, H.; Yang, Y.; Zhang, B. Fractional Vegetation Cover Estimation of Different Vegetation Types in the Qaidam Basin. *Sustain. Switz.* **2019**, *11* (3). https://doi.org/10.3390/su11030864.
31. Ghobadi, Y.; Pradhan, B.; Shafri, H. Z. M.; Kabiri, K. Assessment of Spatial Relationship between Land Surface Temperature and Landuse/Cover Retrieval from Multi-Temporal Remote Sensing Data in South Karkheh Sub-Basin, Iran. *Arab. J. Geosci.* **2015**, *8* (1), 525–537. https://doi.org/10.1007/s12517-013-1244-3.
32. Flocas, H.; Kelessis, A.; Helmis, C.; Petrakakis, M.; Zoumakis, M.; Pappas, K. Synoptic and Local Scale Atmospheric Circulation Associated with Air Pollution Episodes in an Urban Mediterranean Area. *Theor. Appl. Climatol.* **2009**, *95* (3–4), 265–277. https://doi.org/10.1007/s00704-008-0005-9.
33. climate-data.org. *climate-data*. climate-data.org (accessed 2023-04-10).
34. Norman, J. M.; Becker, F. Terminology in Thermal Infrared Remote Sensing of Natural Surfaces. *Agric. For. Meteorol.* **1995**, *77* (3–4), 153–166. https://doi.org/10.1016/0168-1923(95)02259-Z.
35. Sobrino, J.; Raissouni, N.; Li, Z.-L. A Comparative Study of Land Surface Emissivity Retrieval from NOAA Data. *Remote Sens. Environ.* **2001**, *75* (2), 256–266.
36. Malakar, N. K.; Hulley, G. C.; Hook, S. J.; Laraby, K.; Cook, M.; Schott, J. R. An Operational Land Surface Temperature Product for Landsat Thermal Data: Methodology and Validation. *IEEE Trans. Geosci. Remote Sens.* **2018**, *56* (10), 5717–5735. https://doi.org/10.1109/TGRS.2018.2824828.
37. Stathopoulou, M.; Cartalis, C. Daytime Urban Heat Islands from Landsat ETM+ and Corine Land Cover Data: An Application to Major Cities in Greece. *Sol. Energy* **2007**, *81* (3), 358–368. https://doi.org/10.1016/J.SOLENER.2006.06.014.
38. Pal, S.; Ziaul, S. Detection of Land Use and Land Cover Change and Land Surface Temperature in English Bazar Urban Centre. *Egypt. J. Remote Sens. Space Sci.* **2017**, *20* (1), 125–145. https://doi.org/10.1016/J.EJRS.2016.11.003.
39. Chakraborty, T. C.; Lee, X.; Ermida, S.; Zhan, W. On the Land Emissivity Assumption and Landsat-Derived Surface Urban Heat Islands: A Global Analysis. *Remote Sens. Environ.* **2021**, *265*. https://doi.org/10.1016/j.rse.2021.112682.
40. Rubio, E.; Caselles, V.; Badenas, C. Emissivity Measurements of Several Soils and Vegetation Types in the 8-14 Mm Wave Band: Analysis of Two Field Methods. *Remote Sens. Environ.* **1997**, *59* (3), 490–521. https://doi.org/10.1016/S0034-4257(96)00123-X.
41. Stamou, A.; Patias, P. Analyzing the Relationship between Urban Patterns and Land Surface Temperature Using Worldview-2 and LANDSTAT-ETM+". *J. Earth Sci. Eng.* **2014**, *4* (4), 195–202.
42. Do Nascimento, A. C. L.; Galvani, E.; Gobo, J. P. A.; Wollmann, C. A. Comparison between Air Temperature and Land Surface Temperature for the City of São Paulo, Brazil. *Atmosphere* **2022**, *13* (3). https://doi.org/10.3390/atmos13030491.
43. Kawashima, S. Relations between Surface Temperature and Air Temperature on a Local Scale during Winter Nights. *J. Appl. Meteorol.* **2000**, *39*, 1570–1579.
44. Unger, J.; Gál, T.; Rakonczai, J.; Mucsi, L.; Szatmári, J.; Tobak, Z.; Van Leeuwen, B.; Fiala, K. Air Temperature Versus Surface Temperature In Urban Environment. In *The seventh International Conference on Urban Climate*; Yokohama, Japan, 2009.

45. Weng, Q.; Lu, D.; Schubring, J. Estimation of Land Surface Temperature-Vegetation Abundance Relationship for Urban Heat Island Studies. *Remote Sens. Environ.* **2004**, *89* (4), 467–483.
46. Chen, X. L.; Zhao, H. M.; Li, P. X.; Yin, Z. Y. Remote Sensing Image-Based Analysis of the Relationship between Urban Heat Island and Land Use/Cover Changes. *Remote Sens. Environ.* **2006**, *104* (2), 133–146. https://doi.org/10.1016/j.rse.2005.11.016.
47. Guan, K. K. *Surface and Ambient Air Temperatures Associated with Different Ground Material: A Case Study at The*; 2011.
48. Yang, J.; Zhan, Y.; Xiao, X.; Xia, J. C.; Sun, W.; Li, X. Investigating the Diversity of Land Surface Temperature Characteristics in Different Scale Cities Based on Local Climate Zones. *Urban Clim.* **2020**, *34*, 100700. https://doi.org/10.1016/J.UCLIM.2020.100700.
49. Ayanlade, A.; Aigbiremolen, M. I.; Oladosu, O. R. Variations in Urban Land Surface Temperature Intensity over Four Cities in Different Ecological Zones. *Sci. Rep.* **2021**, *11* (1). https://doi.org/10.1038/s41598-021-99693-z.
50. Liu, S.; Su, H.; Zhang, R.; Tian, J.; Wang, W. Estimating the Surface Air Temperature by Remote Sensing in Northwest China Using an Improved Advection-Energy Balance for Air Temperature Model. *Adv. Meteorol.* **2016**, *2016*. https://doi.org/10.1155/2016/4294219.
51. United Nations - Department of Economic and Social Affairs. *United Nations - Sustainable Development Goals*. https://sdgs.un.org/goals. https://sdgs.un.org/goals (accessed 2023-04-10).